University of Plymouth

PEARL **https://pearl.plymouth.ac.uk**

Faculty of Science and Engineering School of Engineering, Computing and Mathematics

2018-11

A laboratory experiment on the incipient motion of boulders by highenergy coastal flows

Bressan, L

http://hdl.handle.net/10026.1/11880

10.1002/esp.4461
Earth Surface Processes and Landforms
Wiley

All content in PEARL is protected by copyright law. Author manuscripts are made available in accordance with publisher policies. Please cite only the published version using the details provided on the item record or document. In the absence of an open licence (e.g. Creative Commons), permissions for further reuse of content should be sought from the publisher or author.

A laboratory experiment on the incipient motion of boulders by high-energy coastal flows

Bressan L., Guerrero M., Antonini A., Petruzzelli V., Archetti R., Lamberti A., Tinti S.

Keywords: boulder transport, hydraulic experiment, transport initiation, instability conditions

Accepted Article

Abstract

Studies on coastal boulders transported inland by high-energy events, as tsunamis, focus mainly on the nature, magnitude and characteristics of past events and contribute to coastal hazard assessments. However, uncertainties on the transport models used in the literature are widely acknowledged.

To study the minimum flow conditions for boulders transport, a laboratory experiment was carried out at the Hydraulic Engineering Laboratory (LIDR) of the University of Bologna, Italy. The main objective was to provide experimental data on boulders incipient motion and on the relationships linking boulders weight, geometry and orientation with the flow velocity and flow depth thresholds for transport initiation. The experiments reproduce idealized cases to highlight the contribution of the flow and transport processes, while the complexities due to the environment and irregular boulder shapes are reduced to a simple slope and to cubic and rectangular blocks.

This article has been accepted for publication and undergone full peer review but has not been through the copyediting, typesetting, pagination and proofreading process which may lead to differences between this version and the Version of Record. Please cite this article as doi: 10.1002/esp.4461

This article is protected by copyright. All rights reserved.

The most important result is that boulders move when only partially submerged by the flow, despite this case is not even considered in the literature. Even for this oversimplified case, the hydrodynamic approach currently used to predict incipient motion strongly overestimates the minimum conditions for boulder transport. The main conclusions are that the drag and lift coefficients commonly used in the literature are not adequate to correctly estimate the minimum conditions for transport and need to be fine-tuned. The main reason for this discrepancy is that the practical hydrodynamic formulas do not account for the flow variability induced by turbulence that plays a key role in influencing the start of instability. To take into account this intrinsic uncertainty, we suggest to determine two dynamic thresholds, separating three distinct regimes: one where the transport is impossible, one where it is certain, and an intermediate one where it is possible depending only on the actual turbulence bursts.

Data are made freely available (ftp://137.204.48.34).

1. Introduction

The importance of studies on coastal boulders related to marine hazards, such as tsunamis, storms and typhoons, is attested by a wide topical literature: boulders transported onshore, even of considerably large size, have been found on many coasts worldwide, as reported in numerous scientific works (see for example the list in Table 1). At first, these were called tsunami boulders since their transport was ascribed to tsunamis, which were believed to be the only extreme marine events capable to dislocate huge and very heavy blocks. However, after boulders transport by storms and typhoons was confirmed in many cases (Mastronuzzi and Sansò, 2004,

This article is protected by copyright. All rights reserved.

Scicchitano et al., 2007, Hall et al., 2008, Etienne and Paris, 2010, Cox et al., 2012, May et al., 2015, Naylor et al., 2016, May et al., 2015, Kennedy et al., 2016), the term “tsunami boulder” cannot be considered appropriate anymore. Nonetheless, it is still used and it will be used also here to denote “onshore-transported boulders”.

It is known that tsunami boulders can provide clues on the magnitude and return period of the extreme marine events responsible for their transport, which is essential for coastal marine hazard assessments (Terry et al., 2016). Studies regarding boulders transport can be grouped mainly in two complementary categories. On one side, there are geological investigations on boulder deposits, where the focus is on boulder weight and geometry classification, boulder origin and initial position, detachment mechanism, transport occurrence time and source type. Usually, in these studies, use is made of hydrodynamic formulas that take into account all mechanical forces and torques acting on the boulder (weight, friction and fluid forces: drag, lift, inertia) and provide the minimum flow velocity and/or flow depth capable of boulders mobilization. The first model was developed by Nott (1997) and later noticeable variants were proposed, among others, by Benner et al. (2010) and Nandasena et al. (2011b). This approach has the advantage to be simple and easy to use, but also the disadvantage to assume strong approximations for boulder geometry and setting, and for flow properties. Generally, boulders are supposed to be homogeneous rectangular prisms. Moreover, the environment-boulder interaction is represented by a friction coefficient, which crudely simplifies the complexity of rocky and/or stony beaches. Furthermore, the flow-boulder interaction is synthesized by means of drag and lift coefficients (and in some cases also by means of the added mass), which are difficult to estimate and could be affected by large uncertainties.

The complementary approach is the use of numerical models that compute not only

This article is protected by copyright. All rights reserved.

the mobilization conditions, but the full process of boulders transport by the water flow. Imamura et al. (2008) simulated the transport of two big boulders by the 1771 Meiwa (Japan) tsunami, while Goto et al. (2010b) and Nandasena et al. (2011a) simulated the boulders transport induced by the 2004 Indian Ocean catastrophic tsunami. Further, experimental laboratory tests (Imamura et al., 2008; Nandasena and Tanaka, 2013) were used to validate numerical models for boulders transport. This combination of numerical and experimental methods to study past events is currently the most accurate method, although it cannot be adopted if the marine event responsible for the transport is unknown.

The goal of this paper is to present a laboratory set of experiments of boulders transport by tsunamis where the assumptions commonly adopted in the hydrodynamical formulas in literature are respected, i.e. the approximations of the environment-boulder interaction is represented by a friction coefficient and boulders are homogeneous cubes or rectangular prisms. The main objective is to provide data for the incipient motion of boulders having different shape, setting and weight induced by surges covering a variety of flow conditions, and to compare experimental data against the results obtained by computing the flow conditions theoretically, as illustrated in the next section.

2. Hydrodynamic equations for prismatic boulders instability

In the hydrodynamic approach, the study of the incipient motion is based on the limit equilibrium conditions of all forces and torques acting on the boulder. Boulders start moving when the balance either of forces or torques or both is broken. From this starting point, different authors develop threshold conditions for incipient motion for

This article is protected by copyright. All rights reserved.

flow velocity and/or flow depth. In this paper we follow the concepts and notation by Nandasena et al. (2011b), though some of their assumptions are modified to account for partially submerged boulders. This approach is simple and suitable for this experiment, since it describes the balance conditions in a general way without introducing assumptions on the flow depth and velocity and their relationships (excluding the one that the flow velocity is depth averaged), which would be superfluous since they are both measured in the tests. On the other hand, more complicated approaches taking into account turbulent peak velocity durations and impulses (see Celik et al.'s study, 2010, of grain entrainments for sand-sized material), or the effects of local roughness on boulders dislodgement (see Weiss and Diplas, 2015), have not been considered since, in the specific experimental setting of this paper, the block doesn't need to overcome an obstacle or to come out of a niche to start moving.

The assumptions made in this study are listed in the following:

1) the boulder lies on a flat plane inclined at an angle θ.
2) the boulder is initially in a dry region and then is hit by a water flow;
3) the boulder is isolated and detached from the underlying substrate;
4) the initial motion of boulder has no components in the transversal direction (i.e. along the horizontal axis perpendicular to the water flow).
5) the forces playing a role are gravity, drag, lift, buoyancy and bottom resistance and, in virtue of (3), they lie all in a vertical plane;
6) the inertial force is neglected, since the steepness of the water front is negligible and considered horizontal.
7) the torque has only one component along the transversal direction and causes

This article is protected by copyright. All rights reserved.

rotation around the rear edge of the boulder;

8) the flow velocity is depth-averaged;

A scheme is shown in Fig. 1.

It is assumed that the boulder transport process is initiated if any of the balances breaks down. Mathematically, this is expressed by means of the following two inequalities, where M_R and R denote the resistive torque and force respectively; D and L are the drag and lift forces exerted by the water flow; $F_\perp$ and $F_\parallel$ designate the components of the force F perpendicular and parallel to the flow direction:

1. When the water impacts the block, the flow tends to turn the boulder around the rear bottom edge, which breaks the balance between the drag and lift torques on one side and the resistive weight torque on the other, and a rotational motion is started when:

$$M_D + M_L > M_R, \quad (1)$$

2. When the water hits the block, the boulder is lifted, which consequently reduces the bottom friction and, with it, the resistive force, so that the boulder is dragged by the fluid, which breaks the balance of the forces in the direction of the flow, and a translational motion is started:

$$D > R_\parallel \quad (2)$$

The lift force and the corresponding torque acting on a partially submerged boulder can be expressed as:

$$L = 0.5\, \rho_w\, C_L\, A_{wbs}\, v^2, \quad (3a)$$

$$M_L = b_L\, L. \quad (3b)$$

Likewise, the drag force and torque can be given the expressions:

$$D = 0.5\, \rho_w\, C_D\, A_{wfs}\, v^2, \quad (4a)$$

This article is protected by copyright. All rights reserved.

$$M_D = b_D\, D. \quad (4b)$$

In eqs. (3) and (4) ρ_w is the water density, C_L and C_D are the lift and drag coefficients. Further A_{wbs} is the area of the wet bottom surface, A_{wfs} the area of the wet front surface, v the depth-average water velocity, and b_L and b_D the moment arms of the lift and drag forces.

The torque that acts against the boulder motion is related to the weight W:

$$M_R = b_W\, W, \quad (5)$$

where b_W is the lever arm. The effective weight W of a partially submerged boulder of volume V, and its components in the parallel and perpendicular flow directions can be given as follows:

$$W = gV\,(\rho_s - \rho_w V_w/V), \quad (6a)$$

$$W_{\parallel} = W \sin\theta, \quad (6b)$$

$$W_{\perp} = W \cos\theta \quad (6c)$$

with g the gravity acceleration, ρ_s the boulder density, V_w the wet volume and θ the slope angle.

After substituting expressions (3) and (4) in the inequality (1), one gets:

$$0.5\,\rho_w\, b_D\, C_D\, A_{wfs}\, v^2 + 0.5\,\rho_w\, b_L\, C_L\, A_{wbs}\, v^2 > b_W W.$$

From this, it is easy to see that the minimum flow velocity v_M needed to break the torque equilibrium and to cause rotation is given by:

$$v^2 > \frac{2\, b_W W}{\rho_w\,(b_D\, C_D\, A_{wfs} + b_L\, C_L\, A_{wbs})} = v_M^2. \quad (7)$$

Before starting the analysis of the translational stability of the block it is convenient to introduce the dynamic pressures:

This article is protected by copyright. All rights reserved.

$$P_k = \frac{\rho_w}{2} v_k^2 = \frac{W_{\parallel} + k\, W_{\perp}}{C_D\, A_{wfs} + k\, C_L\, A_{wbs}}, \quad (8a)$$

$$P_D = \frac{\rho_w}{2} v_D^2 = \frac{W_{\parallel}}{C_D\, A_{wfs}}, \quad (8b)$$

$$P_L = \frac{\rho_w}{2} v_L^2 = \frac{W_{\perp}}{C_L\, A_{wbs}}, \quad (8c)$$

In the definition (8a), k denotes the static friction coefficient. It can be shown that P_k lies always between P_D and P_L and that the above pressure values either satisfy the inequality chain:

$$P_D < P_k < P_L, \quad \text{and analogously,} \quad v_D^2 < v_k^2 < v_L^2 \quad (9a)$$

or the opposite one:

$$P_L < P_k < P_D \quad \text{and analogously,} \quad v_L^2 < v_k^2 < v_D^2 \quad (9b)$$

Usually the experimental conditions are such that the chain (9a) holds (see Appendix for proof). This is the case for the experimental setting of the present paper. This study, for simplicity, will only consider case 9a.

After the above premise, let's consider that the forces opposing the boulder motion are due to the effective weight W and the static bottom friction F_S:

$$R_{\parallel} = W_{\parallel} + F_S, \quad (10)$$

with

$$F_S = \max (k (W_{\perp} - L), 0) \quad (11)$$

It is convenient to carry out the mobilization analysis distinguishing two cases, namely the cases of $F_S=0$ and $F_S>0$.

This article is protected by copyright. All rights reserved.

The static friction F_S is zero if $L > W_\perp$, which becomes $0.5\,\rho_w\,C_L\,A_{wbs}\,v^2 > W_\perp$ after using eq.(3a). This implies that the bottom friction reduces to zero only if the bottom surface is at least partially wet ($A_{wbs} \neq 0$) and this can be expressed in terms of the velocity threshold v_L as follows:

$$v^2 > \frac{2\,W_\perp}{\rho_w\,C_L\,A_{wbs}} = v_L^2 \qquad (12a)$$

Since from the inequality of the dynamic pressures (9a) it follows that $v_D < v_L$, the boulder is unstable if the flow velocity fulfills the relationship $v^2 > v_L^2$.

On the other hand, if $F_S>0$ (i.e. if $0 < v^2 < v_L^2$), then, according to (2), the instability occurs when the following inequality is satisfied:

$$0.5\,\rho_w\,C_D\,A_{wfs}\,v^2 > W_\parallel + k\,(W_\perp - 0.5\,\rho_w\,C_L\,A_{wbs}\,v^2)\,,$$

that is when:

$$v^2 > \frac{2\,(W_\parallel + k\,W_\perp)}{\rho_w\,(C_D\,A_{wfs} + k\,C_L\,A_{wbs})} = v_k^2 \qquad (12c)$$

Considering the inequalities (9a), from which it descends $v_k < v_L$, one concludes that v_k is the minimum speed for the flow to cause the block to translate.

Combining the results of the rotational and translational analyses, the instability condition for the flow velocity will be:

$$v^2 > \min(v_M^2, v_k^2), \qquad (13)$$

This article is protected by copyright. All rights reserved.

where v_M is the incipient velocity threshold found from the torques balance and v_k the threshold velocity resulting from forces balance.

The relationships between the flow velocity v and the flow depth h at the incipient motion are presented for a cubic block in Fig. 2. The dependence of v on h comes from b_L, b_D, b_w, A_{wfs}, A_{wbs} and V_w (and therefore also W), which vary with the flow when the block is only partially submerged and are constant in case of total submergence. In the results, the flow depth is reported along the block edge and is normalized to the block height ($h_n = h/h_{boulder}$), so that for h_n=1 the water covers all the frontal surface, but the upper surface is still dry.

3. Laboratory experiments set-up

To identify the hydraulic conditions of boulders incipient motion, an experiment was conducted at the Hydraulic Engineering Laboratory (LIDR) of the University of Bologna. The transport of a solid object by a fluid flow depends on the object, flow and environment characteristics. In this study, the problem was simplified by considering the incipient motion of regular blocks under various and flow conditions on a homogeneous and gentle-slope plane.

The laboratory experiments consisted in a series of tests conducted in an 11 m long and 0.5 m wide flume. The flow was obtained by generating a dam-break bore, i.e. by quickly opening a gate of a 2.0 m long water tank placed at one end of the flume. The bore runs along the first part of the flume, which is flat and smooth, then climbs up a constant and homogenous slope where it hits the boulder, and, after reaching the maximum height, flows back towards the generation tank. Gauges measure the flow

This article is protected by copyright. All rights reserved.

velocity and depth while the boulder position is controlled by a high-frequency camera to check its state of rest (Fig. 3).

Different tests were carried out by varying flow conditions and block characteristics. Conceptually, in all tests the flow properties depend only on the water depth in the generation tank. Four blocks of different shape, two of approximately cubic shape (C1 and C2) and two rectangular prisms (R1 and R2), and of different weight were positioned at different orientations with respect to the flow direction (see Table 2 and Fig. 4). By referring to the angle α between the mean flow direction and the unit vector normal to the frontal face of the block, blocks C1 and C2 were set at α=0° and α=45°, causing the flow to hit respectively the block face and its edge. Similarly, rectangular-base blocks R1 and R2 were placed with the longer side lying on the slope at α=0°, α=45° and α=90°, corresponding to the flow hitting the larger face, the leading edge and the smaller face of the block, respectively. A list of symbols is provided in Table 3.

Each test was performed by taking the following measurements (see Fig. 3):

- the bore passage downstream of the generation tank, by making use of three water level gauges installed along the flume longitudinal axis. These gauges are transducers that detect the bore passage as an electrical signal connected to the resistance change induced by transducers wetting. From these measurements, the mean velocity of the bore propagation was retrieved;
- the along-flume component of the flow velocity at the slope base, by using an ultrasonic Doppler velocimeter (UDV) with the acoustic beam aligned with the flume axis;
- the rest and motion condition of the block, by using a 100 fps camera;

This article is protected by copyright. All rights reserved.

- the velocity of the flow hitting the block, by combining two UDVs that measure the flow velocity in front of the boulder along two independent directions within the flume longitudinal plane;
- the depth of the flow in front of the block, by analyzing the echo levels from the UDV beam perpendicular to the slope (see next section for details);
- the boulder movement track by using two 33 fps cameras.

The tests were grouped in series. In the first test of each series the height of the water in the tank was taken so low that the flow was unable to destabilize the block. Tests were then repeated by increasing the tank water height by predefined small amounts up to reaching the minimum level to generate a flow capable of moving the boulder.

3.1. The UDV system

The experiments were run by using a system of three ultrasonic Doppler velocimeters (UDVs), designated by DV1, DV2 and DV3 (Fig. 3A and 3B). UDVs are devices that emit ultrasound directional pulses and receive the pulse reflected by scattering particles (DOP2000). The measured frequency shift (Doppler effect) between emitted and received pulses is due to the velocity of the scattering particles transported by the flow, which yields the flow actual velocity. DV1 was employed to measure a velocity profile at the beginning of the slope, while DV2 and DV3 were installed in front of the boulder so that the velocity components measured along the DV2 and DV3 beams allowed to compute the flow velocity vector in the flume longitudinal plane: one acoustic beam (DV3) was set perpendicular to the slope surface pointing upwards and the other (DV2) was set at an angle of 20° with DV3.

The UDV measures a detailed profile of the flow velocity component in the beam

This article is protected by copyright. All rights reserved.

direction: DV2 and DV3 were able to render respectively 65 and 88 mm long profiles with a 0.6 and 1.3 mm resolution. Since individual profiles are affected by the randomness of the scattering process, each profile was sampled eight times and averaged to limit the noise. It is worth noting that the three transducers (DV1, DV2 and DV3) were used in multiplexing mode within the same UDV system: for every acquisition, the UDV system switches between the three DVs that measure the velocity profile one at a time. This method gave an average 14 Hz acquisition frequency for each velocity profile.

4. Data processing

4.1. Flow velocity and flow depth in front of the boulder

The flow velocity component aligned with the slope is the most relevant variable for our study because it is related to the drag force moving the boulder. To obtain it, one needs to measure the flow velocity along two independent directions within the flume longitudinal plane, which was accomplished by using transducers DV2 and DV3. Observe that the transversal component of the flow velocity vector is not relevant because of the quasi-two-dimensional experimental set-up.

The velocities parallel to the slope appeared extremely noisy and characterized by strong spatial (along the beam profile) and temporal variations reflecting a chaotic feature of the generated bore (see Fig. 4). Temporal changes might also be partially ascribed to the lack of full simultaneity of the UDV signal acquisition due to multiplexing.

The average parallel-to-slope velocity of the flow in front of the boulder v(t) was estimated by averaging the velocities along the vertical profile and by smoothing the

This article is protected by copyright. All rights reserved.

temporal variations: first, a depth averaged velocity $v_h(t)$ was calculated, which was further filtered in time with cubic smoothing splines to obtain the average velocity v(t). A measure of the spatial variation $\delta v_h(t)$ is obtained by computing the standard deviation of the velocities along the UDV beam profile with respect to $v_h(t)$, while the corresponding measure of the temporal variation $\delta v_t(t)$ was estimated by computing the standard deviation of v_h with respect to v(t), on a fixed-length time window centered on t (see Fig. 4).

The flow depth along a vertical axis at 2 cm from the boulder was derived by identifying the distance corresponding to the scattering of the water surface in the DV3 recording. This was possible since the water surface acts as a reflective surface producing a clear peak of echo intensity. Notice that, since the DV3 beam is normal to the slope, the echo peak corresponds to a distance along the beam, which was converted to a vertical distance by simple projection. The acoustic assessment of water depth was calibrated against images acquired in specific preliminary tests. In these tests, a laser beam lighted the water surface and the slope at the flume longitudinal central axis, which were filmed by the 100 fps camera pointing perpendicular to the flume at one side (Fig. 3A and 3B).

4.2. Detection of the incipient motion

The time of the incipient motion of a block was determined by carefully inspecting the snapshots sequence taken by the 100 fps camera, and by detecting the first frame where the boulder was displaced from its initial position. This was possible with an accuracy of 0.01 sec. Once the time was known, one could determine the corresponding flow depth and velocity.

Because of the high variability of the flow, the block initial motion could be ascribed to

This article is protected by copyright. All rights reserved.

a turbulence burst rather than to the mean flow velocity. Hence in the following the experimental results are presented in two forms, that is by considering either *i)* the average flow velocity v(t), or *ii)* the peak velocity (see Fig. 4). This latter was estimated as $v_p(t)=\max(v(t)+ \delta v_t(t), v_h(t)+ \delta v_h(t))$.

4.3. Turbulence estimation

Since turbulence is critical for the instability conditions of the block, a quantification of the instantaneous turbulence energy TE is useful and may be obtained by means of the following considerations. We introduce here the total turbulent kinetic energy by means of $v_h(t)$, i.e. by $TKE \approx 0.5\ \rho_w\ v_h(t)^2$, and likewise for the kinetic energy of the steady flow, i.e. $KE = 0.5\ \rho_w\ v(t)^2$. Consider further that the expected value of $E(v_h(t))$ is v(t), by definition. By virtue of this, one can write:

$$\delta v_t^2 = \mathrm{E}\left((\mathrm{v_h(t)} - \mathrm{v(t)})^2\right) \cong \mathrm{E}\left(\mathrm{v_h^2}\right) - \mathrm{v}^2,$$

then obtaining a way to estimate TE, i.e. $TE = 0.5\ \rho_w\ \delta v_t^2 \approx$ TKE-KE.

4.4. Incipient motion diagrams

The results of our tests are shown by means of incipient-motion (or instability) plots where for each experimental run the non-dimensional square velocity of the flow, measured at the instant when the block starts moving, is plotted vs. the corresponding non-dimensional measured flow depth (see Figs. 5-7). In all these graphs, the depth of the flow is taken along the block edge and it is normalized to the height of the boulder, namely $h_n = h/h_{boulder}$. Notice that the boulder is completely submerged for $h > h_S = h_{boulder} + a\tan(\theta) > h_{boulder}$, i.e. for $h_n > h_S/h_{boulder} > 1$ (with *a* the horizontal distance occupied by the boulder in the direction of the flow and θ the slope angle). For our

This article is protected by copyright. All rights reserved.

experiments, $h_{boulder}$ is almost the same for all blocks (see Table 2). The square flow velocity v_n^2 is made adimensional by means of the product of the gravity acceleration g times the block height $h_{boulder}$, i.e. $v_n^2 = v^2/(g\, h_{boulder})$.

In all instability plots, the experimental observations are compared to the theoretical curves of the hydrodynamic model that are obtained by expressing the instability velocities v_n^2 derived from Eq. (13) as a function of h_n. It is relevant to observe that, to compute such curves, the values used for the boulder side lengths and weight and for the slope-block friction coefficient were measured (Table 2), while the water density and the drag and lift coefficients were retrieved from the literature and are displayed in Table 4. For partially submerged blocks, we decided to make use of typical values of drag coefficients for pillars (2d structures) and, when blocks are totally underwater, of drag coefficients for both 2d and 3d structures.

5. Experimental results

Experimental results are given in terms of average and peak velocities next to each other in Fig. 5, left and right panels, for tests involving the cubic blocks C1 and C2, and analogously in Fig. 6 for tests with the rectangular-base blocks R1 and R2.

The first important findings are that most of the experimental data-points in the graphs are found in the region of $h_n < 1$ and below the theoretical curves. This means that the block transport process starts generally well before blocks are completely submerged by the flow, in contrast with the assumptions usually made in the literature, and for flow velocities that are much smaller than the ones predicted by the hydrodynamic model.

This article is protected by copyright. All rights reserved.

Looking at the instability graphs, one may notice that experimental data exhibit a wide velocity spread for similar conditions (i.e. for similar depths, block type, weight and orientation) that is about of the same order of magnitude as the velocity itself. Nonetheless, considering the region of partially submerged blocks, one can observe that for lower flow depths a higher velocity is needed to move the block and that such visible decreasing trend seems in general to go in parallel with the theoretical curve, i.e. it seems that v_n^2 decreases similarly as $1/h_n$. In the following sections, the results for the cubic blocks and the rectangular-base blocks are discussed separately.

5.1. Cubic blocks

From the average-velocity plots (see left panels of Fig. 5), blocks C1 and C2 start moving when the flow covers respectively only 30% and 40% of their height. The minimum non-dimensional square velocity found for instability ranges between 0.02 and 0.1 (corresponding to laboratory velocities of 0.1 and 0.2 m/s) against a much higher theoretical value of about 0.5 and 0.7 (corresponding to velocities of 0.4 and 0.5 m/s). The average velocity curves overestimate observations (more for block C1 than for block C2, for which the theoretical curves approach the upper limit of the experimental data) and decrease slightly slower than experimental data.

The comparison between the average- and the peak-velocity instability graphs (right panels) shows a significant difference. If the peak velocity is considered, all experimental data are shifted expectedly upward, and, as a consequence, lie closer to the theoretical curves. The best agreement holds for the flow hitting blocks with a α=45° orientation. For an α=0° orientation, theoretical curves are seen to bound the upper limit of the experimental data region.

This article is protected by copyright. All rights reserved.

5.2. Rectangular blocks

The results for the rectangular blocks R1 and R2 (see Fig. 6) exhibit a behavior that is partly similar to, but under some relevant aspects, also different from the outcomes for blocks C1 and C2. Considering the average-velocity instability plots (left panels), the blocks start moving when the flow covers only about 40% of the block height for all orientations. The weights of the blocks R1 and R2 are quite different, and expectedly data show that larger velocities are needed to move the heavier block. The instability velocity spread is quite large and the theoretical curves tend to overestimate the observed velocities.

Results depend strongly on the block orientation, which makes it possible to identify a disadvantageous orientation for motion: the threshold velocity happens to be much higher when the flow hits the smaller face of the block, i.e. when the block is aligned with the flow (90° orientation). As for R1, the minimum value for the normalized square velocity is about 0.02, 0.06 and 0.4 respectively for 0°, 45° and 90° orientations (corresponding to values 0.1, 0.1 and 0.4 m/s respectively), while for R2 it is of about 0.04, 0.07 and 2.0 (corresponding to about 0.2, 0.2 and 0.8 m/s).

Unexpectedly, R1 and R2 show a different behavior between 0° and 45° orientation. Block R1 starts moving for smaller velocities when it is oriented at 0°, with the largest face against the flow, while block R2 is more easily transported (it requires smaller velocities) when it is oriented at 45°, with the flow hitting the edge, which is especially true for the low-flow-depth regime. Since blocks differ from one another only for density and hence for weight, this discrepancy is difficult to explain. A factor playing a possible role is the asymmetric shape of the blocks. Indeed, for block R2 in 45° orientation, the drag forces acting on the right and left faces are unbalanced, so that the block is first

This article is protected by copyright. All rights reserved.

rotated by the flow and then transported. This mechanism, implying the block rotation around the axis normal to the slope as the primary source of instability, is not accounted for by the hydrodynamic model illustrated in this paper and it requires further testing.

By examining more carefully the results obtained for the different block orientations, one sees that the instability velocities exhibit a large spread for all orientations and a marked dependence on the flow depth h_n. For the 90° orientation, the pattern is clear for block R1, with the instability velocity decreasing with depth at a rate larger than the theoretical curve, while, for block R2, the few data-points cover a region with square velocities v_n^2 between 2.0 and 3.0 (corresponding to 0.8-0.9 m/s) and with flow depth h_n between 0.4 and 0.8. The only exception are the 0° orientation data that tend to cluster when h_n is slightly larger than 1.0 for block R1. These data, corresponding to the case when the flow surface touches the upper face of the block, can probably be explained through a different mechanism of motion initiation, since the flow generates a standing wave right after the block.

If one takes into account the graphs with the peak velocities (see right panels of Fig. 6), one observes that the theoretical curves in general are closer to the clouds of the experimental points, which confirms the previous results for blocks C1 and C2. However, there are still a significant number of data falling below the curves, which means that the model still overestimates the observed instability conditions.

5.3. Comparison of cubic and rectangular blocks

In Fig. 7, the effects of different shape and volume are shown for blocks C1 and R1, which are approximately of the same density. The two blocks differ mainly for one

This article is protected by copyright. All rights reserved.

dimension that makes R1 about twice as large as C1, so that R1 in the 0° and in 90° orientation can be seen as the sum of two adjacent blocks of type C1. The most relevant observation is that C1 and R1 experimental data tend to agree for the orientations of 0° and 45°, but block R1 exhibits also data with larger velocities, especially in the areas of h_n>1.

6. Principal Component Analysis

Since the incipient motion data form a rich dataset, we carried out a statistical analysis to summarize the different causes of the instability conditions. For this purpose, a principal components analysis (PCA) has been performed by considering the following variables: average velocity v_n, flow depth h_n, angle of attack α, turbulent energy TE, block weight W.

Their composition is shown in the top panels of Fig. 8, together with the percentage of the variance explained by each pc. The component pc1 explains the 35% of the variance and noticeably presents high and similar weights for v_n, h_n and α, larger than for the other variables. The negative coefficient for the flow depth h_n reflects the inverse relationship between flow velocity and depth. The component pc2 explains the 29% of the variance and takes into account all variables with similar coefficient magnitudes, with the weight of the boulder as the main contributor. The third component pc3 (18% of the variance) is clearly dominated by the turbulent energy TE. Further, pc4 describes how the flow depth, boulder's weight and orientation interact with each other. Eventually, pc5 explains only the remaining 5% of the variance. Summarizing, the PCA reflects the complexity of the phenomenon and of the intertwined dependencies, since all variables come into play in the composition of each pcs. In Fig. 8a-8f, the dataset is shown by means of projections on various planes of

This article is protected by copyright. All rights reserved.

the pcs space, which are not trivial to interpret. One can observe that in Fig. 8d, the dataset is clearly arranged along lines depending on orientation α and weight W, while maintaining variability along the sub-vertical direction, roughly parallel to TE, v_n and h_n. In Fig. 8a and 8c it is also visible a clustering due to the boulder weight W.

7. Discussion

The main result coming from our experiments regards the facts that 1) instability involves not only fully underwater boulders but also boulders that are partially submerged by the attacking flow, 2) theoretical curves computed under the assumption of steady flow conditions substantially overestimate the velocity thresholds, 3) experimental data are characterized by a large spread. This triggers a number of comments. The first one is the utilization of inadequate values for the lift and drag coefficients to compute the theoretical relationships for the cases taken into consideration in this paper. We believe that a more detailed knowledge of the instability processes is needed and specific tests should be devised to evaluate such coefficients for the problem of the initiation of boulders transport.

More importantly, the discrepancy between data and the hydraulic model can be due to turbulence, which can be invoked to explain the points 2) and 3) above. We observe that the experimental flows of the incipient motion conditions occur either in fully turbulent regime or in transient regime. Indeed, the roughness of the slope ε was in the order of 1 mm, which implies that the relative roughness ε/h of the flows for all experimental runs varied between of 1/30 – 1/100 and guarantees a turbulent flow, with Reynolds number Re(v, h) in the range 10^3 – 3 10^4. This also ensures that the tested flows are realistic and can simulate a high energy coastal inundation.

To test if the mismatch between predicted and observed data points is due to

This article is protected by copyright. All rights reserved.

turbulence, it is interesting to look at the ratio between observed and predicted velocity together with the ratio between the turbulent energy TE estimated from velocity data (through the formula $TE = 0.5\ \rho_w\ \delta v_t^2$) with the kinetic energy of the steady flow KE. Fig. 9 provides graphs for C-type and R-type blocks where theoretical velocities are computed by using the 2d and 3d drag coefficients. The main difference between the 2d and 3d plots is that the maximum limit of the velocity ratio reaches 1.0 for 2d plots and approaches 2.0 for 3d plots. All plots show similar results, that is TE increases by decreasing the velocity ratio and have values of the same or even one order of magnitude higher of KE (TE/KE>1.0). However, for the rectangular blocks plots the spreading of TE/KE is much higher, and, at first glance, the highest TE/KE values correspond to the 0° direction for rectangular blocks.

The unpredictable component associated with turbulence causes an intrinsic variability in the instability conditions, and therefore a wide energy window. This might be regarded as an unavoidable feature. Nonetheless from our results we are able to identify three velocity regions in the incipient-motion plots: namely an upper (high velocity) and lower (low-velocity) regions where boulder mobilization is respectively certain and impossible, separated by an intermediate wide region (with width determined by the spread magnitude) where mobilization may occur. This view could substitute the current method to fix a specific and well defined boundary between stability and instability conditions for tsunami boulders.

For this experimental data (Figs. 5-7), we can estimate the minimum h_n for motion initiation to be around 0.2-0.3 and the minimum instability velocity to be around 0.2 v_{2D} and 0.2 v_{3D}, while the maximum instability velocity is around 1.2 v_{2D} and 2 v_{3D}. This is a first rough estimate of possible ranges of instability conditions, which are however to be used with care, and that need refinement through further studies covering more

This article is protected by copyright. All rights reserved.

general environmental conditions and boulder characteristics. The partition of the graph in the three regions of stability, transition and instability may have a more practical value than a precise boundary between stability and instability, also based on remarks of authors who found the various formulations in the literature too different from one another to be reliably used (see e.g. criticism by Goto et al, 2010a, Bourgeois and MacInnes, 2010, Biolchi, 2016).

In our study we propose instability conditions in terms of flow velocity and flow depth that are measured independently. By changing the volume of water in the tank in our apparatus, we are able to set up tests with different flow velocities and then to measure the corresponding flow depth leading to the block mobilization, arranging the results in instability plots. For natural cases however it is hard to measure at the same time both quantities. Usually, the most available parameter for tsunamis is the water height h, and the particle velocity in the inundation phase may be derived through the approximation $v^2 = g\ h$, as for example in Lorang (2011) and Nott (2003). In our instability graphs, a flooding tsunami is therefore represented by the straight line $v_n^2 = h_n$ that grows from left to right crossing the region of instability. Superposing this line to Figs. 5-7, it straightforward to estimate if a given tsunami is capable of mobilizing boulders of our idealized geometry.

8. Conclusions

The first experimental finding is that boulders can be moved even if only partially submerged by the flow, and hence that it is important not to focus only on cases of fully submerged boulders.

In addition to the average flow velocity and depth, the flow velocity variability was addressed in order to estimate a peak velocity for incipient motion due to the intrinsic

This article is protected by copyright. All rights reserved.

turbulence of the phenomenon. This velocity variability, when the classical approach is used, can be considered an unpredictable component that may have the same order of magnitude as the corresponding average velocity.

The current hydrodynamic approach for incipient motion is found to overestimate the minimum average conditions for boulder motion. Our experimental results highlighted that, for partially submerged boulders, the turbulent component is very significant and that the commonly adopted drag and lift coefficient values fail to satisfactorily represent the data in most cases. Consequently, the current inverse approach, i.e. to deduce information on past events from boulder transport, could lead to results with high uncertainty.

Since it is impossible to reconstruct or recollect the exact conditions especially for past events, the phenomenon has to be studied in its average quantities. The use of velocity and depth ranges for the incipient motion conditions, rather than exact values, could at least take into account the intrinsic variability of the phenomenon.

The experimental results suggest that the hydrodynamic approach of simple formulas is still too inaccurate. The conclusion that the movement of boulders by flows or by waves is to be further studied, and that the common theoretical approach needs to be further refined, is in agreement with the most recent studies of the scientific community (Bourgeois and MacInnes, 2010, Sugawara et al., 2014, Scheffers, 2014, Nandasena, 2015).

Experimental data are made freely available (ftp://137.204.48.34).

Acknowledgements

This article is protected by copyright. All rights reserved.

This work was possible thanks to the support of all personnel of the Hydraulic Engineering Laboratory (LIDR) of the University of Bologna, Italy.

Appendix A

Proof of inequalities of section 2

To prove the expression (9a), let's first compare P_D and P_k. Subtracting (8b) from (8a) and remembering the definitions (6b) and (6c), one obtains:

$$\mathrm{P}_k - \mathrm{P}_D = W\frac{\sin\theta + k\cos\theta}{\mathrm{C}_D\,\mathrm{A}_{wfs} + k\,\mathrm{C}_L\,\mathrm{A}_{wbs}} - W\frac{\sin\theta}{\mathrm{C}_D\,\mathrm{A}_{wfs}} = kW\frac{\mathrm{C}_D\,\mathrm{A}_{wfs}\cos\theta - \mathrm{C}_L\,\mathrm{A}_{wbs}\sin\theta}{\mathrm{C}_D\,\mathrm{A}_{wfs}\,(\mathrm{C}_D\,\mathrm{A}_{wfs} + k\,\mathrm{C}_L\,\mathrm{A}_{wbs})}$$

Likewise, subtracting (8a) from (8c), one gets:

$$\mathrm{P}_L - \mathrm{P}_k = W\frac{\cos\theta}{\mathrm{C}_L\,\mathrm{A}_{wbs}} - W\frac{\sin\theta + k\cos\theta}{\mathrm{C}_D\,\mathrm{A}_{wfs} + k\,\mathrm{C}_L\,\mathrm{A}_{wbs}} = W\frac{\mathrm{C}_D\,\mathrm{A}_{wfs}\cos\theta - \mathrm{C}_L\,\mathrm{A}_{wbs}\sin\theta}{\mathrm{C}_L\,\mathrm{A}_{wbs}(\mathrm{C}_D\,\mathrm{A}_{wfs} + k\,\mathrm{C}_L\,\mathrm{A}_{wbs})}$$

Hence, it is straightforward to see that both above expressions are positive if

$$\tan\theta < \frac{\mathrm{C}_D\,\mathrm{A}_{wfs}}{\mathrm{C}_L\,\mathrm{A}_{wbs}}\,,$$

(A1a)

and that they are both negative if

$$\tan\theta > \frac{\mathrm{C}_D\,\mathrm{A}_{wfs}}{\mathrm{C}_L\,\mathrm{A}_{wbs}}\,,$$

(A1b)

This article is protected by copyright. All rights reserved.

which is the proof of inequalities (9). Notice that the conditions (A1) depend on factors related to the geometry of the experimental setting (slope) and to the shape of the boulder (drag and lift coefficients, wet frontal and bottom areas), but neither on the friction coefficient nor on the dynamic characteristics of the water flow: namely, they are independent from the flow velocity. In the very special case where

$$\tan\theta = \frac{C_D A_{wfs}}{C_L A_{wbs}} \quad \text{(A1c)}$$

then all pressures are equal. Usually the experimental conditions are such that (A1a) holds and that, correspondingly, also the chain (9a) holds.

In the text, the instability conditions of the boulder have been established under the hypothesis that the inequality (A1a) is fulfilled. Here we explore the complementary case (A1b) that implies the dynamic pressures inequalities given by (9b). In turn this is equivalent to assume that:

$$v_L^2 < v_k^2 < v_D^2 \quad \text{(A2)}$$

The stability analysis carried out in the paper is valid also here. Hence, F_S =0 when $v^2 > v_L^2$ (12a) and Fs>0 for flow velocities smaller than v_L. Hence, considering (A2) and the inequalities (12) all together, it is possible to conclude that: 1) for flow velocities below v_L, Fs differs from zero and is large enough to oppose the block motion; 2) for velocities between v_L and v_D, Fs is zero but the block is not able to move; 3) for velocities exceeding v_D, the block is unstable. The consequence is that the condition (13), has to be replaced by the inequality:

$$v^2 > \min(v_M^2, v_D^2), \quad \text{(A3)}$$

This article is protected by copyright. All rights reserved.

As regards the ratio

$$\frac{C_D A_{wfs}}{C_L A_{wbs}} \qquad \text{(A4)}$$

appearing in expressions (A1), we provide here, as an example, an estimate of it under the assumption of a simple-shape boulder lying on a plane of slope θ. Let's consider a block that is a rectangular-based prism with edges *a*, *b* and *c*, where *a* and *b* are transversal and parallel to the water flow respectively and *c* is the height. Hence, the frontal and bottom areas are given by the products *ab* and *ac*. Neglecting the gradient of the flow profile near the block, and measuring the flow depth *h* from the lowest level of the block, the following expressions for the wet bottom surface can be derived:

$$A_{wbs} = \frac{ah}{\sin\theta} \qquad \text{if } h < b\sin\theta \qquad \text{(A5a)}$$

$$A_{wbs} = ab \qquad \text{if } h \geq b\sin\theta \qquad \text{(A5b)}$$

Likewise, the frontal surface is

$$A_{wfs} = \frac{ah}{\cos\theta} \qquad \text{if } h < c\cos\theta \qquad \text{(A6a)}$$

$$A_{wfs} = ac \qquad \text{if } h \geq c\cos\theta \qquad \text{(A6b)}$$

Assuming that $b\sin\theta < c\cos\theta$, which is the case in the laboratory experiments carried out in the present study, the ratio (A4) can be given the following form:

$$\frac{C_D A_{wfs}}{C_L A_{wbs}} = \tan\theta \ \frac{C_D}{C_L} \qquad \text{if } h < b\sin\theta \qquad \text{(A7a)}$$

$$\frac{C_D A_{wfs}}{C_L A_{wbs}} = \frac{hC_D}{b\cos\theta\, C_L} \qquad \text{if } b\sin\theta \leq h < c\cos\theta \qquad \text{(A7b)}$$

$$\frac{C_D A_{wfs}}{C_L A_{wbs}} = \frac{cC_D}{bC_L} \qquad \text{if } c\cos\theta \leq h \qquad \text{(A7c)}$$

Accepted Article

This article is protected by copyright. All rights reserved.

References

Benner R, Browne T, Brückner H, Kelletat D, Scheffers A. 2010. Boulder transport by waves: Progress in physical modeling. Zeitschrift fur Geomorphologie 54 (SUPPL. 3): 127-146.

Biolchi S, Furlani S, Antonioli F, Baldassini N, Causon Deguara J, Devoto S, Di Stefano A, Evans J, Gambin T, Gauci R, Mastronuzzi G, Monaco C, Scicchitano G. 2016. Boulder accumulations related to extreme wave events on the eastern coast of Malta. Natural Hazards and Earth System Sciences 16 (3): 737-756.

Bourgeois J, MacInnes B. 2010. Tsunami boulder transport and other dramatic effects of the 15 November 2006 central Kuril Islands tsunami on the island of Matua. Zeitschrift für Geomorphologie, Supplementary Issues 54(3): 175-195.

Bryant E., Young R and Price D. 1996. Tsunami as a Major Control on Coastal Evolution, Southeastern Australia. Journal of Coastal Research 12(4): 831-840.

Celik A, Diplas P, Dancey C,Valyrakis M. 2010. Impulse and particle dislodgement under turbulent flow conditions. Phys. Fluid 22: 1-13.

Çengel YA, Cimbala JM. 2014. Fluid Mechanics: fundamentals and applications, third edition, McGraw Hill, New York, USA, ISBN: 978-0-07-338032-2.

Costa PJM, Andrade C, Freitas MC, Oliveira MA, Da Silva CM, Omira R, Taborda R, Baptista MA, Dawson AG. 2011. Boulder deposition during major tsunami events. Earth Surf. Process. Landforms 36: 2054–2068.

Courtney C, Dominey-Howes D, Goff J, Chagué-Goff C, Switzer AD, McFadgen B. 2012. A synthesis and review of the geological evidence for palaeotsunamis along the coast of southeast Australia: The evidence, issues and potential ways forward. Quaternary Science Reviews 54: 99-125.

Cox R, Zentner DB, Kirchner BJ, Cook MS. 2012. Boulder ridges on the Aran Islands (Ireland): Recent movements caused by storm waves, not tsunamis. Journal of Geology 120 (3): 249-272.

DOP2000, Model 2125, User's manual (software 2.01, revision 1.0), Signal Processing S.A. Lausanne, Switzerland.

Engel M, May SM. 2012. Bonaire's boulder fields revisited: Evidence for Holocene tsunami impact on the Leeward Antilles. Quaternary Science Reviews 54: 126-141.

Etienne S, Paris R. 2010. Boulder accumulations related to storms on the south coast

This article is protected by copyright. All rights reserved.

of the Reykjanes Peninsula (Iceland). Geomorphology 114(1): 55-70.

Goff J, Nichol S and Kennedy D. 2010. Development of a palaeotsunami database for New Zealand. Natural Hazards 54(2): 193-208.

Goto K, Miyagi K, Kawamata H, Imamura F. 2010a. Discrimination of boulders deposited by tsunamis and storm waves at Ishigaki Island, Japan. Marine Geology 269 (1-2): 34-45.

Goto K, Okada K, Imamura F. 2010b. Numerical analysis of boulder transport by the 2004 Indian Ocean tsunami at Pakarang Cape, Thailand. Marine Geology 268 (1-4): 97-105.

Goto K, Sugawara D, Ikema S, Miyagi T. 2012. Sedimentary processes associated with sand and boulder deposits formed by the 2011 Tohoku-oki tsunami at Sabusawa Island, Japan. Sedimentary Geology 282: 188-198.

Hall M, Hansom JD, Jarvis J. 2008. Processes, patterns and rates of erosion by storm waves on hard rock headlands: the Grind of the Navir, Shetland, Scotland. Marine Geology 248: 28–46.

Hoffmann G, Reicherter K, Wiatr T, Gruetzner C, Rausch T. 2013. Block and boulder accumulations along the coastline between Fins and Sur (Sultanate of Oman): tsunamigenic remains? Nat Hazards 65: 851–873.

Imamura F, Goto K, Ohkubo S. 2008. A numerical model for the transport of a boulder by tsunami. Journal of Geophysical Research 113, C01008. doi:10.1029/2007JC004170.

Kennedy AB, Mori N, Zhang Y, Yasuda T, Chen SE, Tajima Y, Pecor W, Toride K. 2016. Observations and Modeling of Coastal Boulder Transport and Loading during Super Typhoon Haiyan. Coastal Engineering Journal 58 (1): art. no. 1640004.

Kennedy DM, Tannock KL, Crozier MJ, and Rieser U. 2007. Boulders of MIS 5 age deposited by a tsunami on the coast of Otago, New Zealand. Sedimentary Geology 200(3-4): 222-231.

Lorang MS. 2011. A wave-competence approach to distinguish between boulder and megaclast deposits due to storm waves versus tsunamis. Marine Geology *283*(1-4): 90-97.

Maouche S, Morhange C, Meghraoui M. 2009. Large boulder accumulation on the Algerian coast evidence tsunami events in the western Mediterranean. Marine Geology 262 (1-4): 96-104.

This article is protected by copyright. All rights reserved.

Mastronuzzi G, Sansò P. 2004. Large boulder accumulations by extreme waves along the Adriatic coast of southern Apulia (Italy). Quaternary International 120 (1): 173-184.

May SM, Engel M, Brill D, Cuadra C, Lagmay AMF, Santiago J, Suarez JK, Reyes M, Brückner H. 2015. Block and boulder transport in Eastern Samar (Philippines) during Supertyphoon Haiyan. Earth Surf. Dynam. 3: 543-558. doi:10.5194/esurf-3-543-2015.

Medina F, Mhammdi N, Chiguer A, Akil M, Jaaidi EB. 2011. The Rabat and Larache boulder fields; new examples of high-energy deposits related to storms and tsunami waves in north-western Morocco. Natural Hazards 59(2): 725-747.

Nakamura M, Arashiro Y, Shiga S. 2014. Numerical simulations to account for boulder movements on Lanyu Island, Taiwan: Tsunami or storm? Earth, Planets and Space 66 (1): art. no. 128.

Nandasena, NAK. 2015. Inverse modeling of high-energy events: Cliff-edge boulder/block transport by tsunamis. Australasian Coasts & Ports, Auckland, Nw Zealand. 15 September - 18 September 2015. Proceedings of Australasian Coasts & Ports.

Nandasena NAK, Tanaka N. 2013. Boulder transport by high energy: Numerical model-fitting experimental observations. Ocean Engineering 57: 163–179.

Nandasena NAK, Paris R, Tanaka N. 2011a. Numerical assessment of boulder transport by the 2004 Indian ocean tsunami in Lhok Nga, West Banda Aceh (Sumatra, Indonesia). Computers & geosciences 37(9): 1391-1399.

Nandasena NAK, Paris R, Tanaka N. 2011b. Reassessment of hydrodynamic equations: minimum flow velocity to initiate boulder transport by high energy events (storms, tsunamis). Mar. Geol. 281(1): 70-84.

Naylor LA, Stephenson WJ, Smith HCM, Way O, Mendelssohn J, Cowley A. 2016. Geomorphological control on boulder transport and coastal erosion before, during and after an extreme extra-tropical cyclone. Earth Surface Processes and Landforms 41 (5): 685-700.

Nott J. 1997. Extremely high-energy wave deposits inside the Great Barrier Reef, Australia: determining the cause—tsunami or tropical cyclone. Marine Geology 141(1): 193-207.

Nott J. 2003. Waves, coastal boulder deposits and the importance of the pre-transport setting. Earth and Planetary Science Letters 210(1-2): 269-276.

Öğretmen N, Cosentino D, Gliozzi E, Cipollari P, Iadanza A, Yildirim C. 2015. Tsunami hazard in the Eastern Mediterranean: geological evidence from the Anatolian coastal area (Silifke, southern Turkey). Natural Hazards 79 (3): 1569-1589.

This article is protected by copyright. All rights reserved.

Scicchitano G, Pignatelli C, Spampinato C, Piscitelli A, Milella M, Monaco C, Mastronuzzi G. 2012. Terrestrial Laser Scanner techniques in the assessment of tsunami impact on the Maddalena peninsula (south-eastern Sicily, Italy). Earth Planet Sp. 64, 8. doi:10.5047/eps.2011.11.009.

Scicchitano G, Monaco C, Tortorici L. 2007. Large boulder deposits by tsunami waves along the Ionian coast of south-eastern Sicily (Italy). Marine Geology 238(1): 75-91.

Scheffers AM. 2014. Paleotsunami Research-Current Debate and Controversies. Coastal and Marine Hazards, Risks, and Disasters: 59-92.

Shah-Hosseini M, Saleem A, Mahmoud AMA, Morhange C. 2016. Coastal boulder deposits attesting to large wave impacts on the Mediterranean coast of Egypt. Natural Hazards 83 (2): 849-865.

Spiske M, Bahlburg H. 2011. A quasi-experimental setting of coarse clast transport by the 2010 Chile tsunami (Bucalemu, Central Chile). Marine Geology 289: 72-85.

Stephenson WJ, Naylor LA. 2011. Geological controls on boulder production in a rock coast setting: insights from South Wales, UK. Marine Geology 283.1: 12-24.

Sugawara D, Goto K, Jaffe BE. 2014. Numerical models of tsunami sediment transport - Current understanding and future directions. Marine Geology 352: 295-320.

Terry JP, Dunne K, and Jankaew K. 2016. Prehistorical frequency of high-energy marine inundation events driven by typhoons in the Bay of Bangkok (Thailand), interpreted from coastal carbonate boulders. Earth Surf. Process. Landforms 41: 553–562.

Vacchi M, Rovere A, Zouros N, Firpo M. 2012. Assessing enigmatic boulder deposits in NE Aegean Sea: Importance of historical sources as tool to support hydrodynamic equations. Natural Hazards and Earth System Science 12 (4): 1109-1118.

Weiss R, Diplas P. 2015. Untangling boulder dislodgement in storms and tsunamis: Is it possible with simple theories?. Geochemistry, Geophysics, Geosystems 16.3: 890-898.

Accepted Article

This article is protected by copyright. All rights reserved.

Table 1: Examples of tsunami boulder studies.

Ocean/Sea	Region	Reference
Atlantic Ocean	United Kingdom	Stephenson and Naylor, 2011
	Portugal	Costa et al. (2016)
Caribbean Ocean	Bonaire (Leeward Antilles)	Engel and May (2012)
Pacific Ocean	Kuril Islands, Russia	Bourgeois and MacInnes (2010)
	Japan	Goto et al. (2010a, 2012)
	Taiwan	Nakamura et al. (2014)
	Australia	Bryant et al. (1996)
	Australia	Courtney et al. (2012)
	New Zealand	Kennedy et al. (2007)
	New Zealand	Goff et al. (2010)
	Chile	Spiske and Bahlburg (2011)
Indian Ocean	Oman	Hoffmann et al. (2013)
Mediterranean Sea	Italy	Scicchitano et al. (2012)
	Italy	Mastronuzzi and Sansò (2004)
	Malta	Biolchi et al. (2016)
	Greece	Vacchi et al. (2012)
	Turkey	Öğretmen et al. (2015)
	Egypt	Shah-Hosseini et al. (2016)
	Algeria	Maouche et al. (2009)
	Morocco	Medina et al. (2011)

Accepted Article

This article is protected by copyright. All rights reserved.

Table 2: Table of the block properties: weight, dimensions and friction coefficients. Length and width are taken respectively along the slope direction and transversally, assuming 0° block orientation. When orientation is 90°, length and width exchange with each other.

Block	Shape	Dimensions: length, width, height (cm)	Weight (g)	Density (10^3 kg/m^3)	Friction coefficient
C1	Quasi-cube	2.95 x 3.10 x 3.00	53.0	1.9	0.52 ± 0.05
C2	Quasi-cube	3.00 x 2.80 x 3.00	61.0	2.4	0.51 ± 0.06
R1	Rectangular prism	3.10 x 5.45 x 3.00	97.5	1.9	0.65 ± 0.06
R2	Rectangular prism	3.14 x 5.92 x 3.08	150.0	2.6	0.56 ± 0.08

Accepted Article

This article is protected by copyright. All rights reserved.

Table 3: List of symbols.

Variable	Description	units
θ	Inclination angle of the slope	°
D, L and R	Drag, lift and total resistive forces	N
M_D, M_L, M_R	Torques due to drag, lift and resistive forces	Nm
C_D, C_L	Drag and lift coefficients	
v_h	Depth averaged velocity	m/s
v	Average velocity	m/s
v_n	Normalized velocity: $v_n^2 = v^2/(g\, h_{boulder})$	
W	Block weight	kg
α	Angle between the flow direction and the normal to the frontal face of the block	°
v_p	Peak velocity	m/s
TE	Turbulent energy TE≈TKE-KE	J/m^3
v_{th}, v_{2D}, v_{3D}	Theoretical velocity for incipient motion, and velocities computed by using 2d and 3d drag coefficients	m/s
δv_h	Spatial velocity variability, computed as standard deviation of the velocities along the UDV beam profile with respect to v_h	
δv_t	Temporal velocity variability, computed as standard deviation of v_h with respect to v	
k	Friction coefficient	

Accepted Article

This article is protected by copyright. All rights reserved.

Table 4: Lift and drag coefficients used for each block, with references. The 2d drag coefficient for 45° orientation has been chosen as the maximum between the 2d drag coefficients of 0° and 90° orientation, in order to get a smaller and more conservative incipient-motion velocity.

	Value	Block shape	Block orientation	Reference
lift	$C_L = 0.178$	all	all	Nandasena and Tanaka (2013)
drag 2d	$C_D = 2.05$	C1-C2	0°	Çengel and Cimbala (2014)
drag 2d	$C_D = 1.55$	C1-C2	45°	Çengel and Cimbala (2014)
drag 2d	$C_D = 1.7$	R1-R2	0°	Çengel and Cimbala (2014)
drag 2d	$C_D = 2.5$	R1-R2	45°	The higher value between 0° and 90° orientation (see the explanation in the text)
drag 2d	$C_D = 2.5$	R1-R2	90°	Çengel and Cimbala (2014)
drag 3d	$C_D = 1.05$	C1-C2	0°	Çengel and Cimbala (2014)
drag 3d	$C_D = 0.8$	C1-C2	45°	Çengel and Cimbala (2014)
drag 3d	$C_D = 1.95$	R1-R2	0°	Nandasena and Tanaka (2013)
drag 3d	$C_D = 1.95$	R1-R2	45°	Nandasena and Tanaka (2013)
drag 3d	$C_D = 1.95$	R1-R2	90°	Nandasena and Tanaka (2013)

Accepted Article

This article is protected by copyright. All rights reserved.

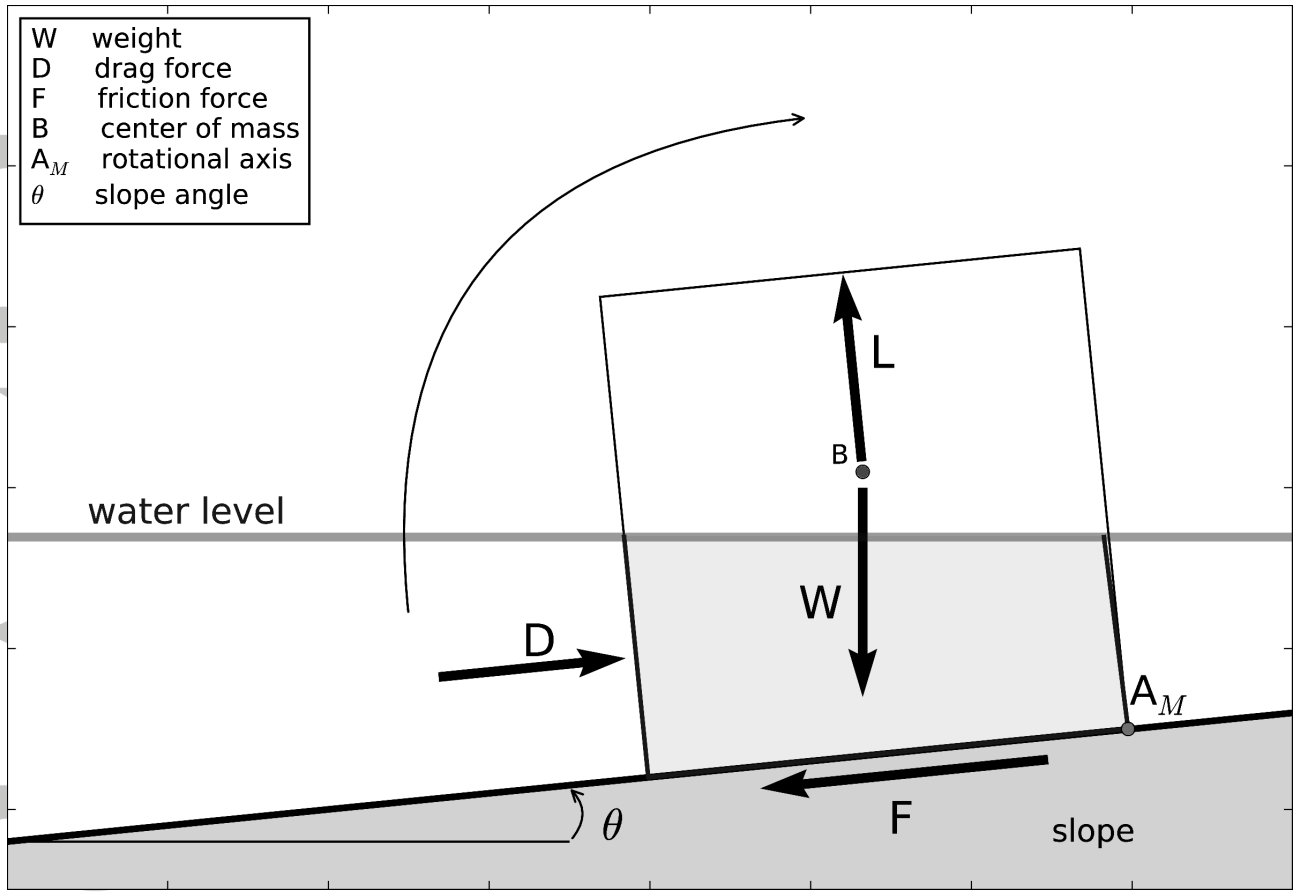

Figure 1. Sketch of forces and torques acting on a partially submerged boulder oriented at α=0° with respect to the flow, with drag (D), lift (L), weight (W) and the static friction force (F). To compute forces and torques balance, all forces are applied at the center of mass B, while all torques are computed with respect to the rotation axis (rear edge) passing through A_M.

Accepted

This article is protected by copyright. All rights reserved.

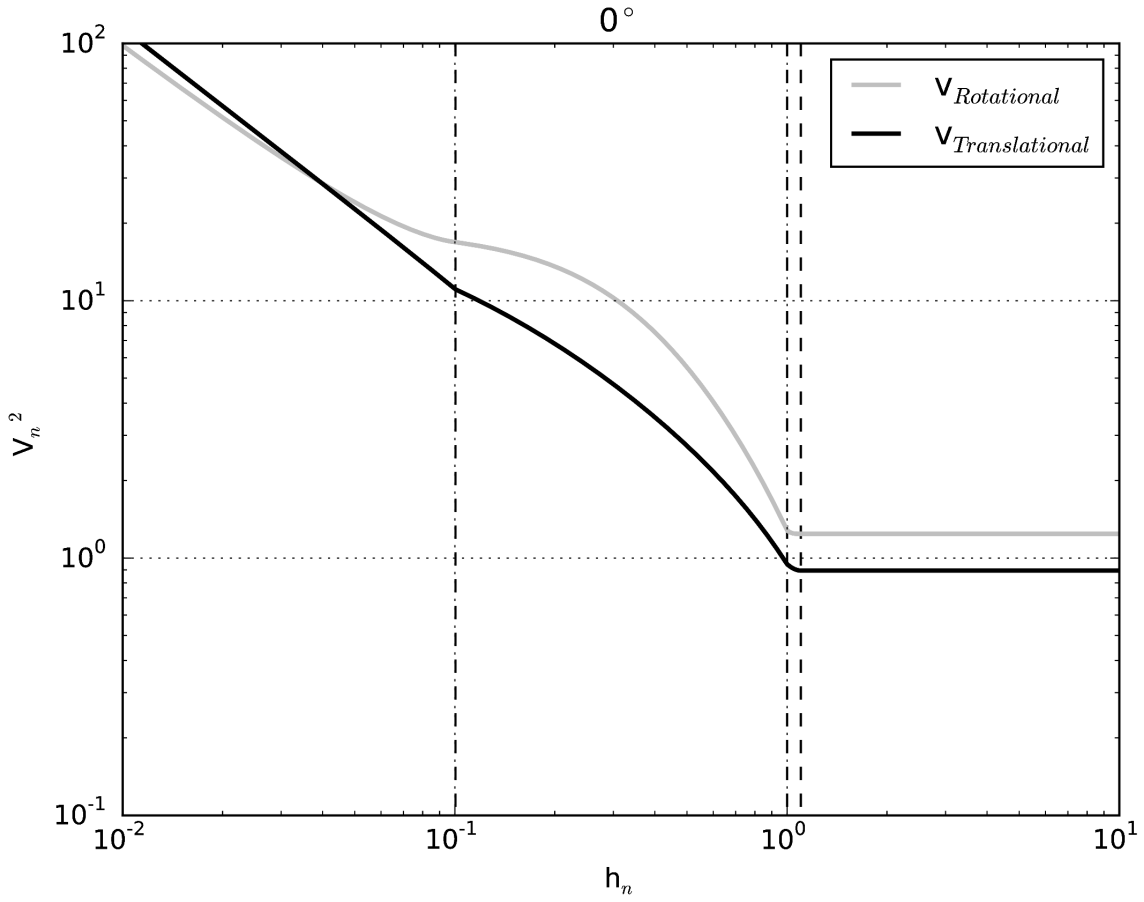

Figure 2: Theoretical curves of the instability velocity for translational (see Eq. 12c) and rotational (see Eq. 7) unbalance, in case of block C1, placed on a beach of slope 1:10, with k = 0.5, C_D = 1.05 and C_L = 0.178. The flow depth h_n is normalized to the side length $h_{boulder}$. The square velocity v_n^2 is also normalized, according to the formula $v_n^2 = v_x^2/(gh_{boulder})$, where the subscript x is either for translational or for rotational instability. The dashed lines mark the flow depth when, respectively, the bottom surface, the front surface and the top surface become completely submerged.

This article is protected by copyright. All rights reserved.

Accepted Article

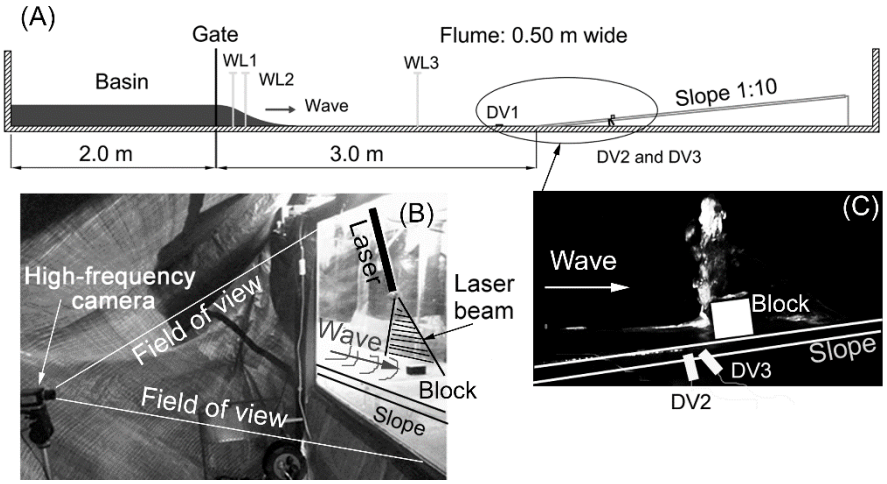

Figure 3. A) Experimental setup: sketched cross-section of the hydraulic flume with the wave generation gate on the left and the wave traveling from left to right. The water level sensors (WL) are placed at distances of 0.16, 0.28 and 1.945 m from the gate (corresponding to the respective distances of 2.935, 2.815 and 1.15 m from the slope base). The Doppler Ultrasound Velocimeter DV1 is placed at 2.7 m from the gate and at 0.4 m from the slope, pointing at the incoming bore. B) Detail of the darkroom along the flume with the high-frequency camera pointing the block from a side window. C) Sideview detail of the block C2 hit by the flow, obtained with the high-frequency camera inside the darkroom and using a laser beam pointing along the axis flume (the DV positions are schematically reported).

This article is protected by copyright. All rights reserved.

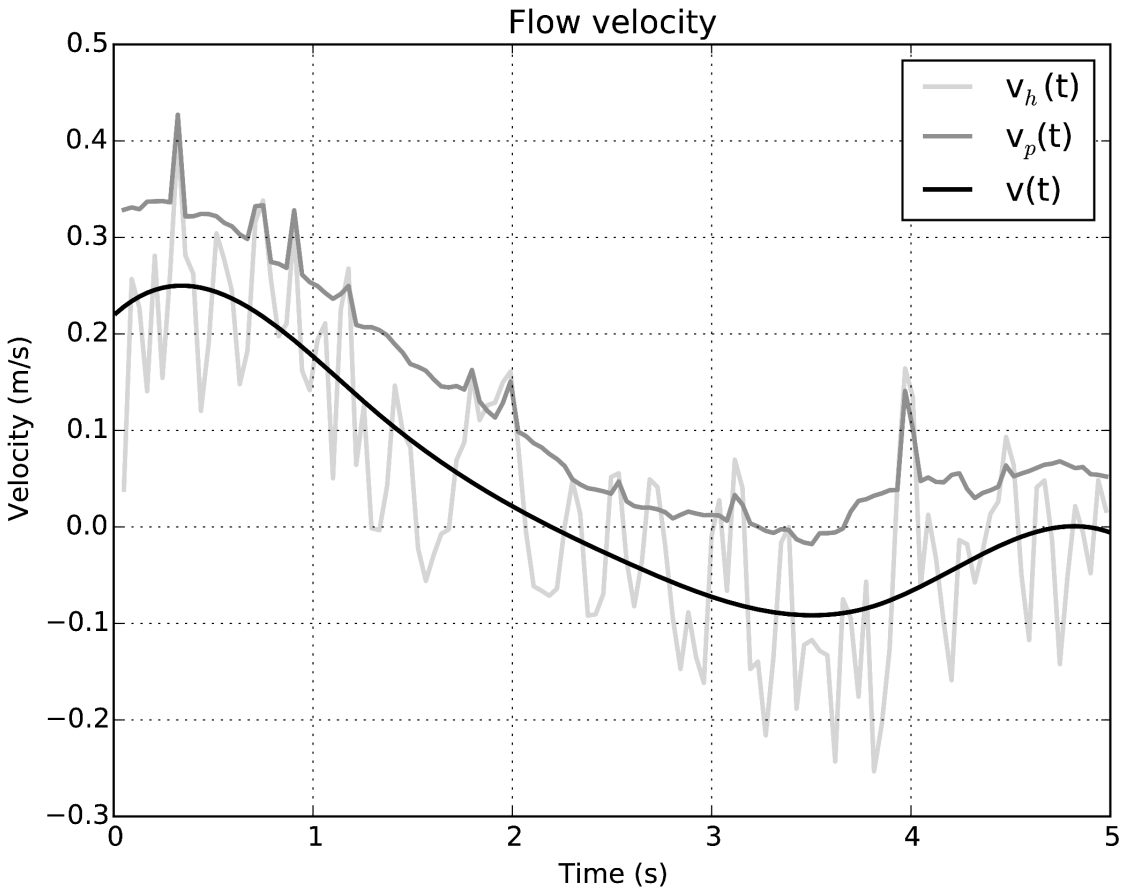

Figure 4. Time series of flow velocity v(t) and v_h(t), and of the peak velocity v_p(t). The average velocity v(t) passes from positive to negative and then vanishes, reflecting the stages of direct (up-slope) and backward (downslope) flow. In the final times (vanishing velocity), the slope is dry again.

Accepted

This article is protected by copyright. All rights reserved.

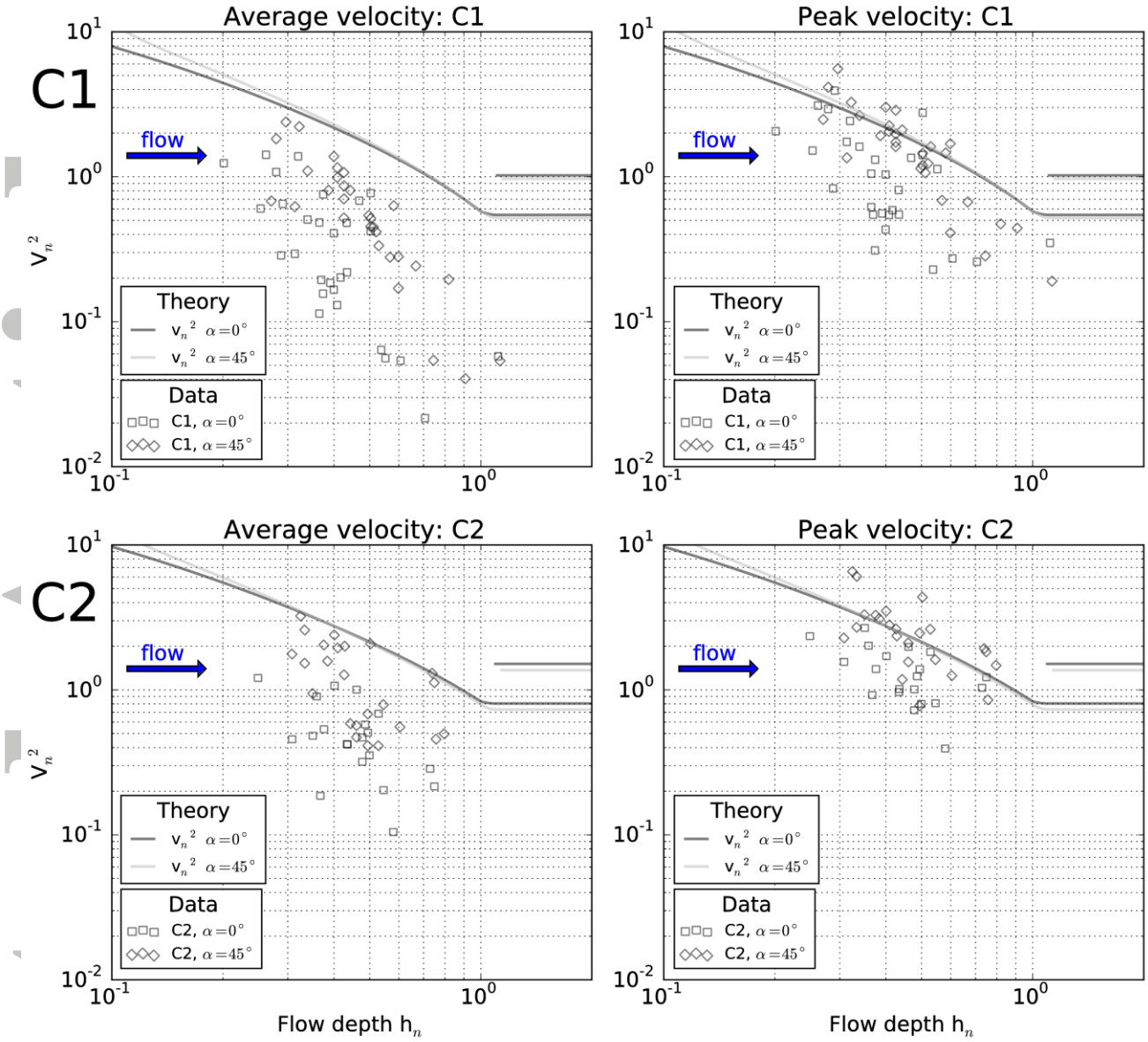

Figure 5. Instability velocity vs. flow depth for the average-velocity (left panels) and the peak velocity (right panels) for blocks C1 and C2 in different orientations. Experimental data are compared to the theoretical instability curves. When blocks are partially submerged curves are computed with 2d-structures drag coefficients. When they are totally underwater, also 3d-structures drag coefficients are used (rightmost part of the graph). The symbols represent the shape and the physical orientation of the block, assuming that the flow comes from the left side.

This article is protected by copyright. All rights reserved.

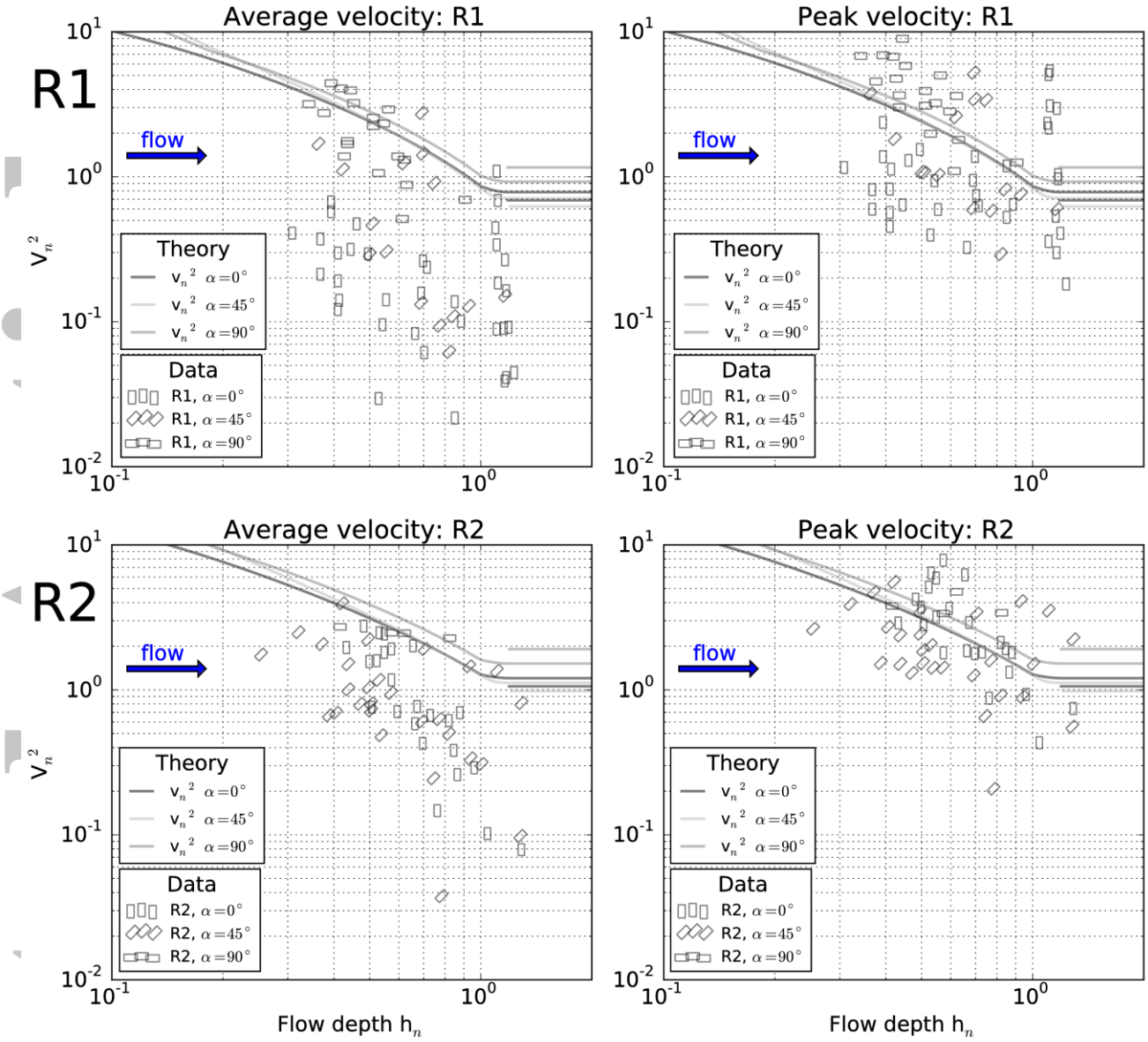

Figure 6. Instability graphs for blocks R1 and R2. For further details, see caption of Fig. 5.

This article is protected by copyright. All rights reserved.

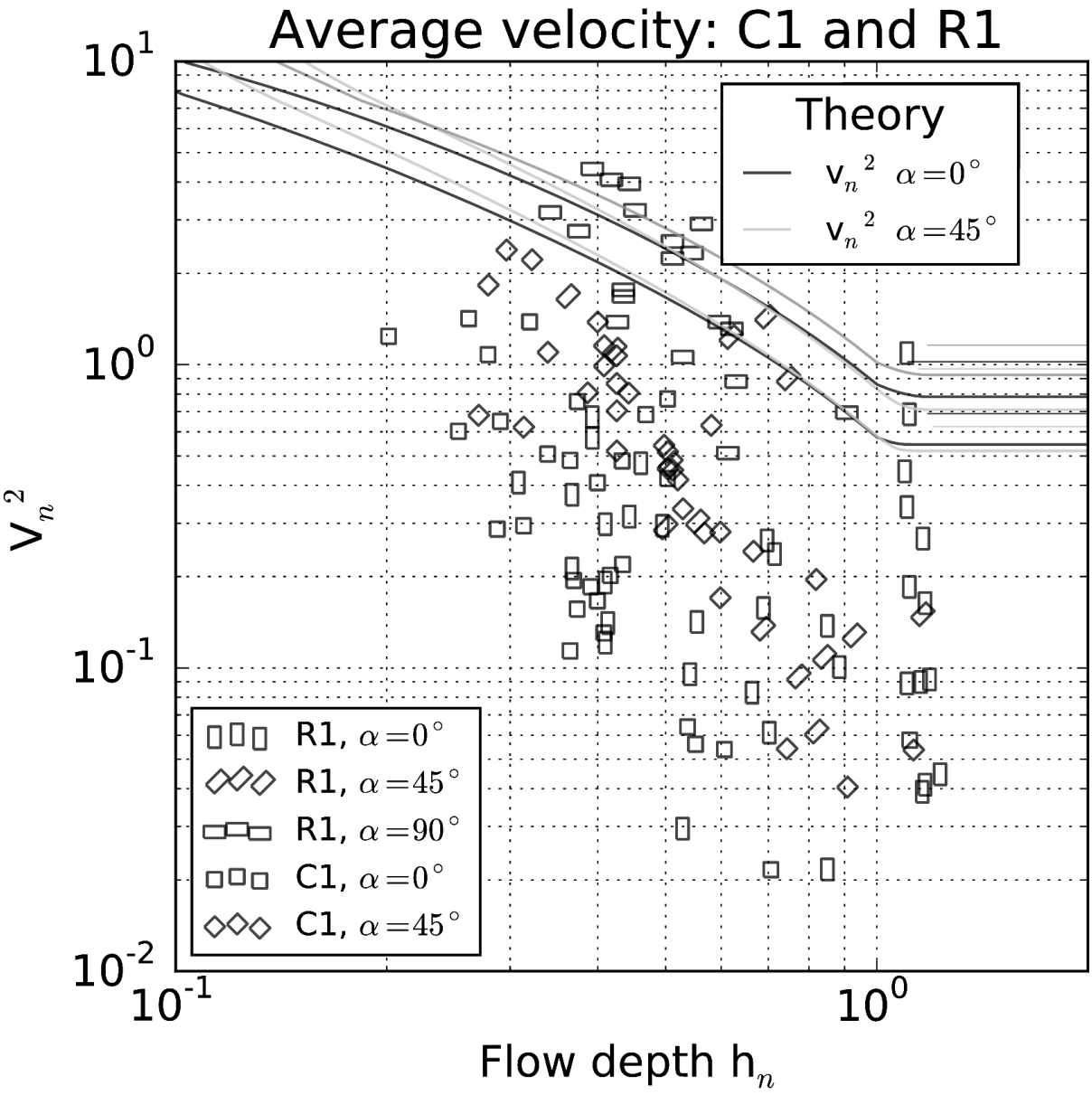

Figure 7. Comparison of the average-velocity instability graphs for blocks C1 and R1. These blocks are approximately the same density and R1 has a volume about twice as large as C1. For further details, see Fig. 5.

This article is protected by copyright. All rights reserved.

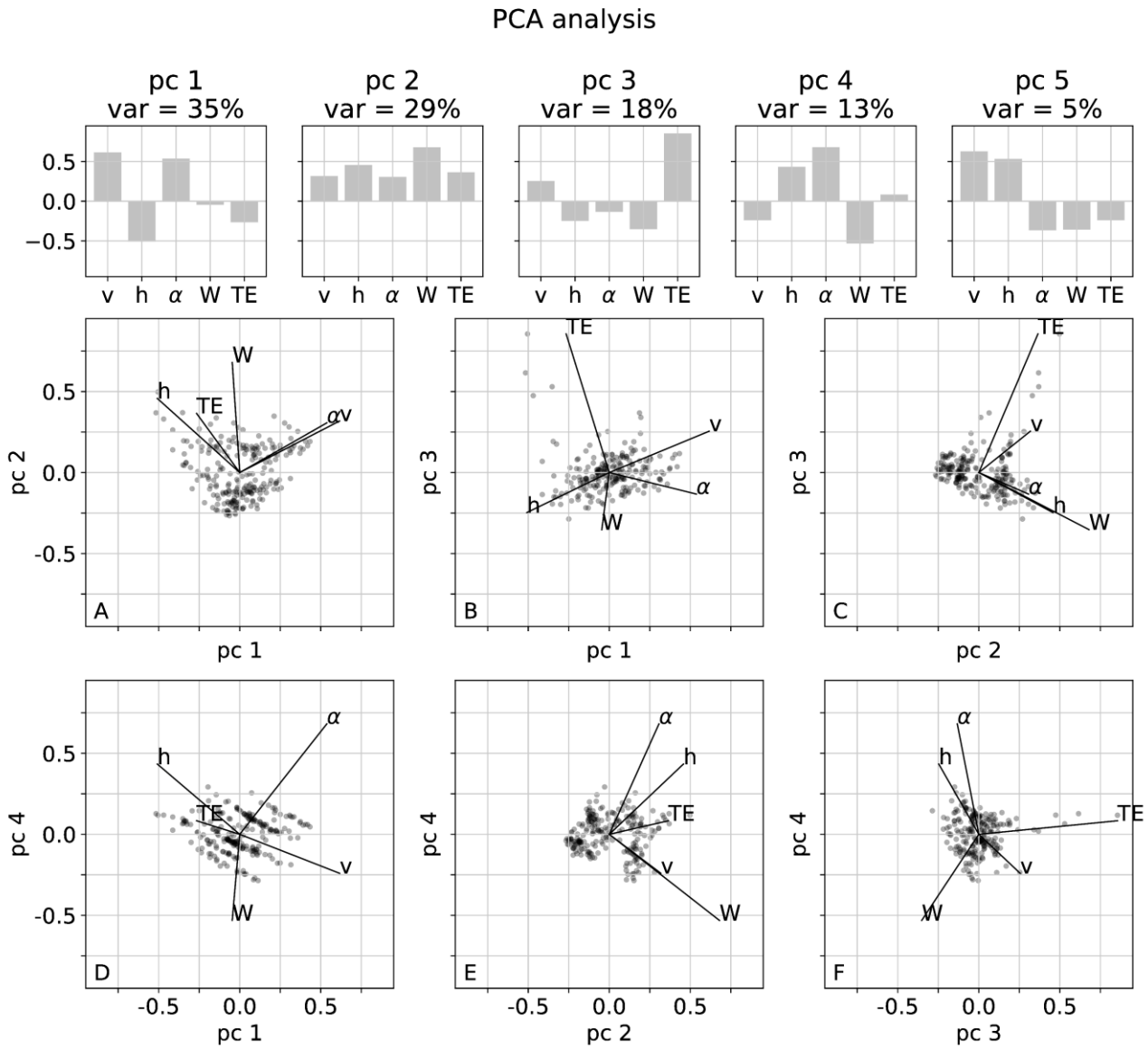

Figure 8. Principal component analysis of the instability conditions dataset. In the top panels, the coefficients of the five principal components in the physical variables space are shown. The other panels show the projection of the whole dataset on two selected pcs.

This article is protected by copyright. All rights reserved.

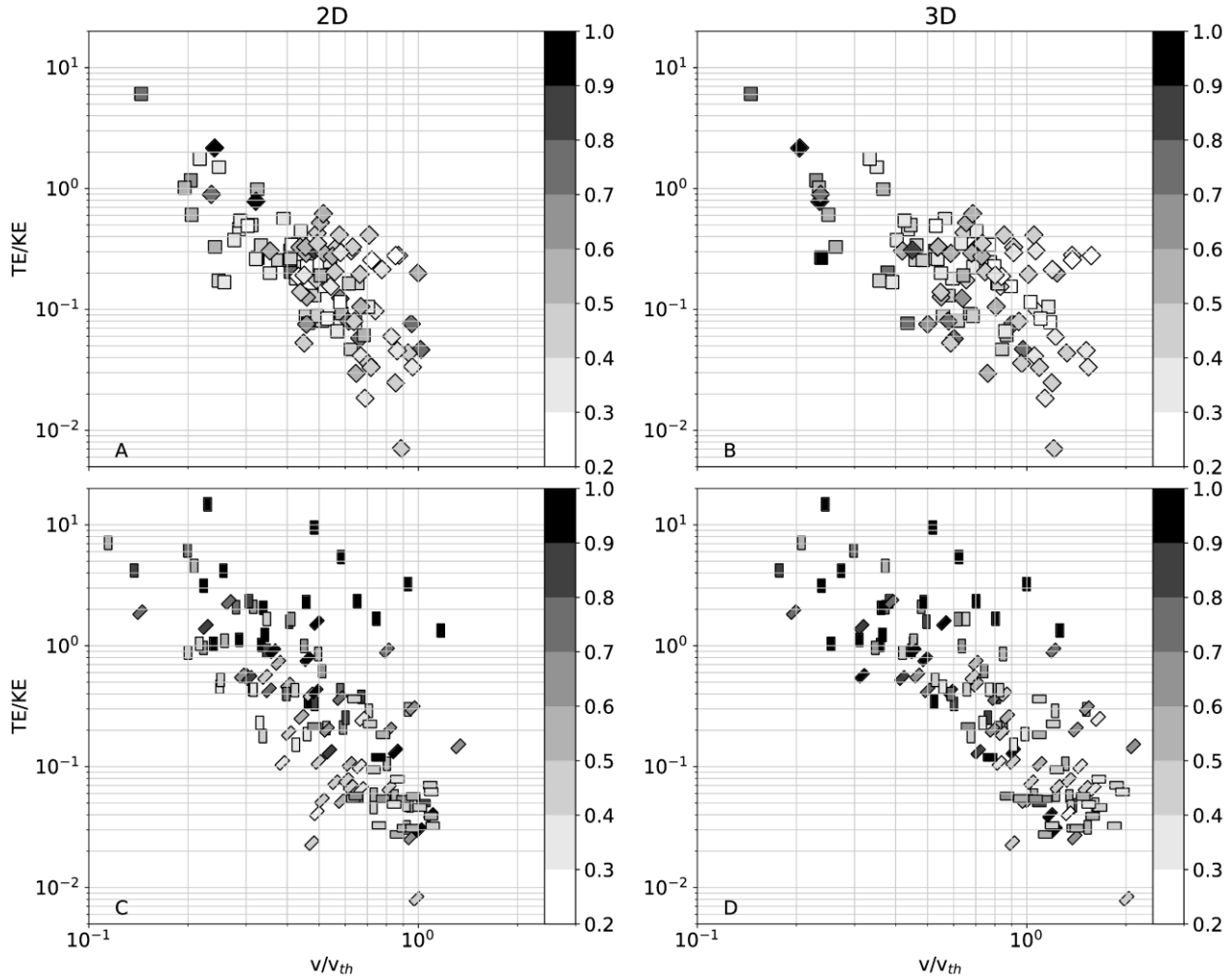

Figure 9. Ratios of steady flow and turbulent kinetic energy TE/KE vs. observed-predicted velocity ratios separately for C1-C2 (top panels) and for R1-R2 blocks (bottom panels), by using the 2d and 3d drag coefficient theoretical velocity, respectively on the left and right panels. The turbulence energy TE is considered to be an approximation of the difference between the total kinetic energy and the kinetic energy of the steady flow (TKE- KE) for incipient motion conditions. The block gray-based colors correspond to h_n according to the color bar shown.

This article is protected by copyright. All rights reserved.

Accepted Article

A laboratory experiment on the incipient motion of boulders by high-energy coastal flows

Bressan L*, Guerrero M, Antonini A, Petruzzelli V, Archetti R, Lamberti A, Tinti S

A laboratory experiment was carried out to study the minimum flow conditions for boulder transport. Boulders move when only partially submerged, furthermore the theoretical predictions for incipient motion overestimates the data, which suggests the need for drag and lift coefficients to be fine-tuned for transport initiation. Since turbulence plays a key role in the instability conditions and causes an intrinsic uncertainty, we propose two thresholds to define hydrodynamics conditions for which the transport is impossible, probable and certain.

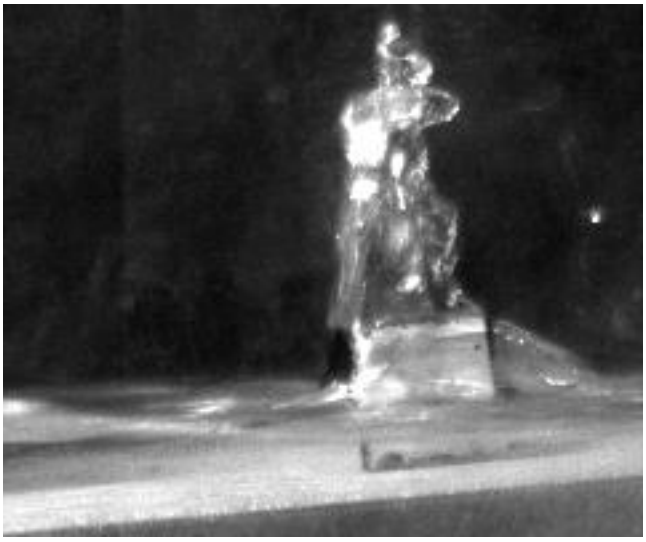

This article is protected by copyright. All rights reserved.